

Two-color interferometry and switching through optomechanical dark mode excitation

David P. Lake, Matthew Mitchell, Barry C. Sanders, and Paul E. Barclay*
*Department of Physics and Astronomy and Institute for Quantum Science and Technology,
University of Calgary, Calgary, AB, T2N 1N4, Canada*

Efficient switching and routing of photons of different wavelengths is a requirement for realizing a quantum internet. Multimode optomechanical systems can solve this technological challenge and enable studies of fundamental science involving widely separated optical wavelengths that are inaccessible to single-mode optomechanical systems. To this end, we demonstrate interference between two optomechanically induced transparency processes in a diamond on-chip cavity. This system allows us to directly observe the dynamics of an optomechanical dark mode that interferes photons at different wavelengths via their mutual coupling to a common mechanical resonance. This dark mode does not transfer energy to the dissipative mechanical reservoir and is predicted to enable quantum information processing applications that are insensitive to mechanical decoherence. Control of the dark mode is also utilized to demonstrate proof-of-principle all-optical, two-color switching and interference with light separated by over 5 THz in frequency.

INTRODUCTION

Interference is a ubiquitous physical phenomenon central to applications ranging from detection of gravitational waves [1] to implementation of modulators essential to telecommunications systems [2], integrated photonics technology [3], and on-chip optical quantum information processing [4]. Each of these examples interfere light at or near the same wavelength to convert differences in phase to changes in intensity. The emergence of frequency bin qubits [5–7] and a desire to interface quantum networking components based on different photonic technologies [8] has created the need for optical devices that interfere light with widely separated frequencies. Typically, this challenge has been addressed using nonlinear atomic [9, 10] or solid-state [11–14] materials, whose microscopic nonlinear optical susceptibility combined with precise photonic dispersion engineering can mediate interactions between different wavelengths of light. Here we demonstrate that cavity optomechanics [15] provides an alternative realization of multi-color optical interference that can be implemented in transparent linear materials through light’s interaction with a nanofabricated mechanical resonator.

By coherently coupling light confined in an optical cavity to motion of a mechanical resonance of the same cavity, light can be slowed and stored [16–18] in a manner analogous to electromagnetically induced transparency [19]. The signature of this coherent optomechanical coupling between phonons and photons is a narrow transmission window in the otherwise opaque optical cavity resonance spectrum, referred to as optomechanically induced transparency (OMIT) [16, 17], whose highly dispersive optical response does not depend on the phase of its input field. In contrast, phase is critically important to the optical properties of multimode optomechanical systems, in which multiple optical fields are injected into a single optomechanical device and interact via their mutual coupling to the mechanical resonator. In the optical

domain, multimode cavity optomechanical devices have been used for experimental demonstrations of wavelength conversion [20–22]. In the radiofrequency and microwave domains multimode devices have enabled low-noise frequency conversion [23] and entanglement between photons [24], whereas hybrid electro-optomechanical devices have used coherent interference between optomechanically and piezomechanically driven motion to bridge microwave and optical frequencies [25]. Optical-frequency optomechanical devices whose intensity response is sensitive to the relative phase of multiple input optical fields with widely separated wavelengths, i.e., that involve interference between different colors of light, have yet to be reported despite proof-of-principle demonstrations based on atomic media [26, 27] and recent advances in cavity optomechanical mediated coupling between multiple mechanical modes [28, 29].

Here we report chip-based cavity optomechanical devices with two optical modes coherently coupled to a single mechanical resonance to show that double optomechanically induced transparency (DOMIT), in which two optical modes coherently transfer energy to the same mechanical mode, enables interference between photons separated by over 5 THz in frequency. This effect manifests as suppression or enhancement of OMIT experienced by an input field at a given wavelength and depends on its phase relative to the input field at a different wavelength. Exploiting this effect, we demonstrate a novel phase-sensitive two-color optical switch that emulates an optical XOR gate [30]. This multi-color interferometry has the remarkable property of persisting even without optomechanically exciting mechanical resonator phonons as the photons interact via a mechanical dark mode [21, 31], which is directly excited for the first time here. Our studies of mechanical dark mode interference of photons without driving motion of the mechanical resonator could enable optomechanical quantum state transfer that is insensitive to mechanical decoherence [31, 32]. Furthermore, the optical XOR gate demonstrated here will be useful

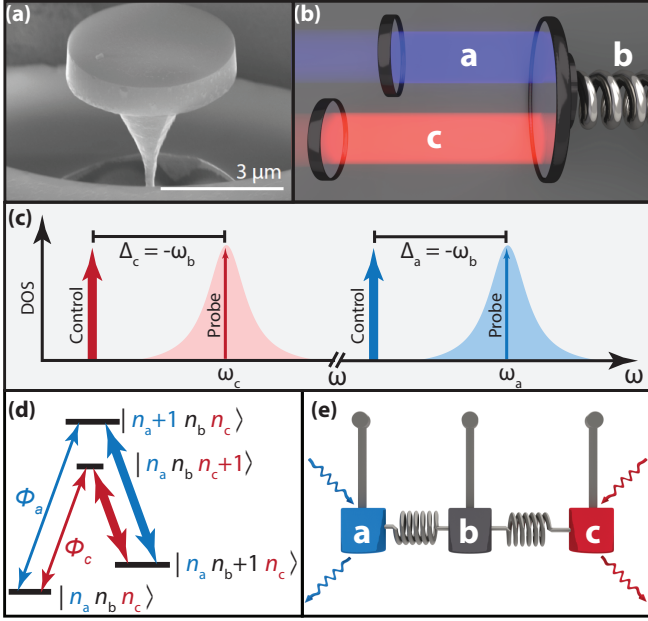


FIG. 1: (a) Scanning electron micrograph of a diamond microdisk similar to the $\sim 5 \mu\text{m}$ diameter one studied in this work. (b) Schematic of a multimode optomechanical system where two Fabry Perot optical modes, a and c , are coupled to the same mechanical mode, b . (c) Frequency-domain illustration of the control and probe lasers used throughout this work, and their respective optical cavity modes. (d) The double- Λ level scheme used in this work, where the labels n_a, n_b, n_c represent the energy levels of modes a, b , and c , respectively. The thick lines represent photon-phonon exchange mediated by the control field, and the thin lines represent the probe fields with phase difference $\phi = \phi_a - \phi_c$. (e) DOMIT can be described by three coupled harmonic oscillators. The optical modes may be driven in-phase, or out-of-phase, exciting either the mechanically bright or the mechanically dark mode.

for multicolor classical and quantum optical information processing, e.g., for demonstrating quantum interference [12, 13] between frequency binned qubits [5–7], as well optical sensing and metrology [14] using interference between widely separated wavelengths.

DOUBLE OPTOMECHANICALLY INDUCED TRANSPARENCY (DOMIT)

Photon-photon interference and mechanical dark mode excitation demonstrated here uses a diamond microdisk cavity optomechanical system (Fig. 1(a)) whose essential elements can be analyzed as a generic Fabry Perot cavity shown in Fig. 1(b). The cavity supports two optical modes with widely separated frequencies ω_a and ω_c , each coupled via radiation pressure to a common mechanical resonator with frequency ω_b established in the generic system by one of the cavity mirrors. Each optical mode is excited with a weak probe field and a strong control laser that is red-detuned from its cavity mode by the mechanical frequency, $\Delta_a = \Delta_c = -\omega_b$, represented

graphically in Fig. 1(c). If the mechanical frequency exceeds the dissipation rate of each optical cavity mode, the system is in the resolved sideband regime, and the interaction Hamiltonian simplifies to [15]

$$\hat{H}_{\text{int}} = -\hbar \left[(G_a \hat{a}^\dagger + G_c \hat{c}^\dagger) \hat{b} + (G_a^* \hat{a} + G_c^* \hat{c}) \hat{b}^\dagger \right], \quad (1)$$

where \hat{a} (\hat{a}^\dagger) and \hat{c} (\hat{c}^\dagger) are the creation (annihilation) operators of the optical probe field photons, \hat{b} (\hat{b}^\dagger) is the creation (annihilation) operator of the mechanical resonator phonons, and we employ the rotating wave approximation. Here $G_a = g_a \alpha_a$ and $G_c = g_c \alpha_c$ are the control-field assisted optomechanical coupling rates for modes a and c , set by the single photon-phonon coupling rates $g_{a,c}$, and the control field amplitudes $|\alpha_{a,c}|^2 = n_{a,c}$. The specific cavity geometry determines $g_{a,c}$, which generally increases as the effective cavity length decreases, whereas the control field amplitudes are set by their intracavity photon numbers $n_{a,c}$, which are typically limited by nonlinear optical effects in the cavity. The system can be described by a double- Λ energy diagram, as illustrated in Fig. 1(d), which forms a closed loop under excitation from the two sets of control and probe fields.

In this DOMIT configuration, each of \hat{a} , \hat{b} , and \hat{c} oscillate in the rotating frame at the same frequency. This allows relative phases between the various fields to be defined, despite their typically vast frequency differences. The key property is that the phases of each of the four fields forming the double- Λ loop affects the optical response [33, 34]. This is in contrast to a single- Λ system, whose optical response depends only on the intensity of the control field. This behaviour is clearly elucidated by studying symmetric and antisymmetric combinations of the cavity's optical modes. These modes are referred to as the 'mechanically dark' ($\hat{C}_{\text{dk}} = (G_c \hat{a} - G_a \hat{c}) / (i\bar{G})$) and 'mechanically bright' ($\hat{C}_{\text{br}} = (G_a^* \hat{a} + G_c^* \hat{c}) / (\bar{G})$) modes, as the dark mode can be entirely decoupled from the mechanical resonator while the bright mode can be maximally coupled; here $\bar{G} = \sqrt{|G_a|^2 + |G_c|^2}$.

These three modes are analogous to the modes of three coupled pendula, as shown in Fig. 1(e), in which the outer two pendula move in opposite directions while the central pendulum is stationary (dark mode); alternatively the three pendula move in the same direction (bright mode). This basis, with analogies in atomic physics [26, 27], elegantly reveals the importance of optical phase to the system's behaviour. The classical amplitudes of the bright and dark modes when both probe fields are resonant with their respective cavity modes are (see Supplemen-

tary Material):

$$\begin{aligned}\zeta_{\text{dk}} &= \frac{2\sqrt{\kappa_{\text{ex}}s_{\text{in}}}}{\kappa} \sin(\phi/2), \\ \zeta_{\text{br}} &= \frac{2\sqrt{\kappa_{\text{ex}}s_{\text{in}}}}{\kappa(1+\overline{C})} \cos(\phi/2),\end{aligned}\quad (2)$$

where κ_{ex} and κ are the external coupling and total loss rates of the cavity modes respectively, s_{in} is the input amplitude of the two probe lasers, $\overline{C} = 4\overline{G}^2/\kappa\gamma_{\text{b}}$ is the two-mode optomechanical cooperativity, and γ_{b} is the damping rate of the mechanical resonance. For simplicity, we assume that κ , κ_{ex} and s_{in} are the same for each optical mode. In our experimental setup, described below, $\phi = \phi_{\text{a}} - \phi_{\text{c}}$ is the phase difference of the probe fields in the rotating frame; as each of the probe fields are derived from their respective control field via electro-optic modulation, changes to the control field phases do not affect the system response.

Equation (2) shows that adjusting ϕ to $\pm\pi$ e.g., by delaying one of the probes, allows complete selective excitation of ζ_{dk} . In contrast, previous experimental studies of dark-modes in wavelength conversion [21] only allow complete dark-mode excitation in the limit $\overline{C} \rightarrow \infty$. When all DOMIT processes are resonant, this delay corresponds to a half period of the mechanical resonator. Equation (2) also shows that full optical power transfer to the dark mode is possible, while the bright mode has a reduced maximum amplitude due to coherent optomechanical transfer of energy to the mechanical resonator. Optically manipulating the system in this basis is central to optomechanical wavelength conversion free from mechanical thermal decoherence effects [31, 32] when the optomechanical coupling exceeds the thermal decoherence rate [20, 21, 35]. However, none of these previous single OMIT studies have completely isolated or selectively populated the mechanically dark mode. Conceptually related studies demonstrating optomechanical control of interference between two mechanical modes [36] have not yet been used to interfere different colors of light.

To demonstrate DOMIT, we evanescently coupled control and probe fields via an optical fiber taper waveguide into modes of a diamond microdisk device similar to that in Fig. 1(a) and previous studies [3, 5]. Our modes have resonant wavelengths $\lambda_{\text{a}} \sim 1520$ nm and $\lambda_{\text{c}} \sim 1560$ nm and sufficiently low optical loss ($\kappa_{\text{a}}/2\pi \sim 0.87$ GHz, $\kappa_{\text{c}}/2\pi \sim 1.20$ GHz) to allow resolved sideband optomechanical coupling to the microdisk's $\omega_{\text{b}}/2\pi = 2.1$ GHz fundamental mechanical radial breathing mode (dissipation rate $\gamma_{\text{b}}/2\pi = 0.285$ MHz). Typical optical and mechanical mode spectroscopy measurements are described in the Supplementary Material. The per-photon optomechanical coupling rates, $g_{\text{a}} = g_{\text{c}} \sim 2\pi \times 25$ kHz, allow optomechanical cooperativity > 1 and observation of OMIT when approximately $n_{\text{a,b}} > 5 \times 10^5$ control photons are coupled into either of the cavity modes [3]. Achieving

this large photon number is possible in our microdisks due to diamond's low nonlinear absorption and excellent thermal properties. In all of our measurements presented below, the input control fields are detuned from their respective cavity modes such that OMIT conditions $\Delta_{\text{a}} = \Delta_{\text{c}} = -\omega_{\text{b}}$ for each mode are satisfied. Note that the microdisks support regularly spaced modes spanning the IR and visible spectrum [5]; our modes are chosen due to the compatibility of their wavelengths with telecommunications equipment needed for the measurements described below.

To excite ζ_{dk} and ζ_{br} , OMIT spectra [3] for modes a and c were recorded for varying relative phase ϕ between the two probe fields, as shown in Figs. 2(a,b). In these measurements, ϕ is controlled by adjusting a delay between two radio frequency (RF) signals split from the same signal generator, which are then used to create the probe fields through optical modulation of two independently running control lasers (see Supplementary Material for details). Our setup is robust to phase drifts of either control laser, as discussed above. Each pair of probe and control fields is isolated by optical filtering and then detected on a high-speed photodetector as a function of varying probe-cavity detuning δ . Each probe amplitude is then measured by downmixing the heterodyne signal that it creates through interference with its corresponding control field using a vector network analyzer. At $\phi = 0$, the deep OMIT window present in each probe output spectrum when $\delta = 0$ indicates excitation of ζ_{br} , whereas, when $\phi = \pi$, the response of the bare cavity, which is broad compared to the OMIT window ($\kappa \gg \gamma_{\text{b}}(1+C)$), is restored for all probe detunings, indicating excitation of ζ_{dk} . The depth of the OMIT window as a function of the phase delay is fit using solutions to Eq. (2) in the a and c basis (see Supplementary Material), and is shown for $\delta_{\text{a,c}} = 0$ in Figs. 2(a,b), where it is seen to agree well with theory.

OPTOMECHANICAL BRIGHT AND DARK MODE COUPLING

When OMIT resonance conditions for both modes are satisfied, i.e., $\Delta_{\text{a}} = \Delta_{\text{c}} = -\omega_{\text{b}}$ and $\delta_{\text{a}} = \delta_{\text{c}} = 0$, the ζ_{br} and ζ_{dk} states are decoupled from each other. However, by incrementing cavity-probe detuning of one mode by $+\delta$, and decrementing cavity-probe detuning of the other mode by $-\delta$, we induce a bright-dark state coupling. This can also be accomplished by shifting Δ_{a} and Δ_{c} in the same manner. Coupling between bright and dark states manifests as a temporal oscillation in the intensity of the probe fields transmitted through the cavity, allowing differences in their interaction with the dissipative mechanical resonator to be observed directly.

Our measurement of both probe colors is plotted in Fig. 3(a), for the case that $2\delta = 3.37$ MHz and $\phi = 0$,

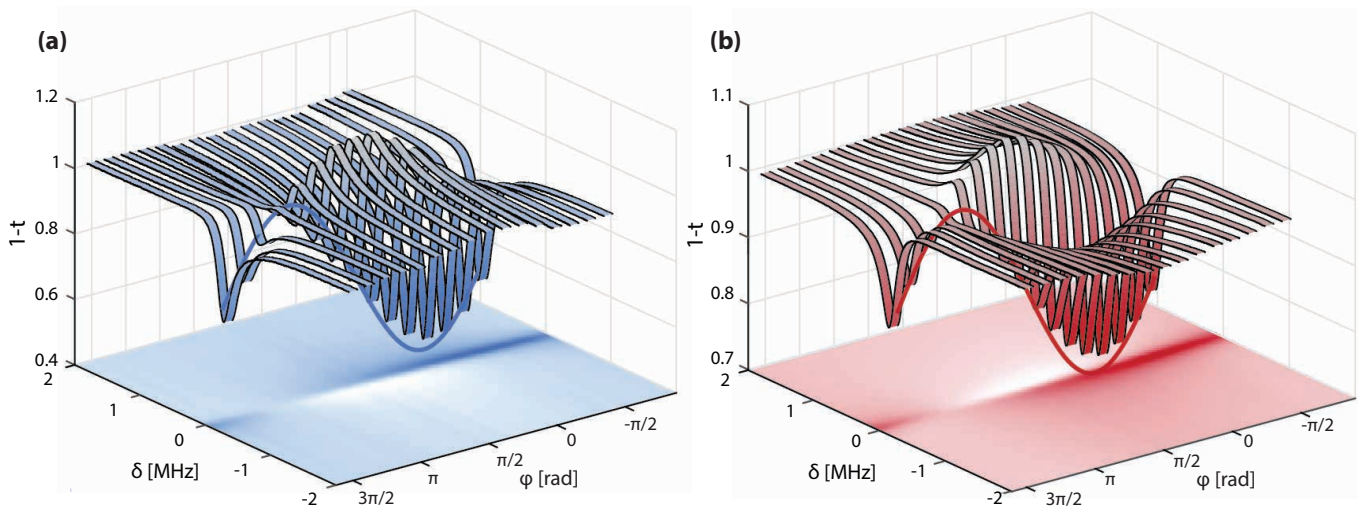


FIG. 2: (a,b) Cavity optical response to the probe signal for modes a and c respectively, as a function of cavity-probe detuning δ , and the probe phase difference ϕ , as recorded by the vector network analyzer from the photodetected heterodyne signal. The control fields are at fixed detuning $\Delta_a = \Delta_c = -\omega_b$.

after digitally downmixing the total (probe and control) photodetected signal from each color recorded on a high-speed oscilloscope to remove fast oscillations near ω_b due to beating between probe and control fields. Each down-mixed signal is proportional to the amplitude, equivalently, the square root of energy, of the intracavity field at its respective probe frequency. As the modulation depth is bounded above by the dark-state transmission (bare cavity response), and bounded below by the bright-state transmission (OMIT window depth), the oscillation amplitude follows the δ dependence of the OMIT features. This dependence is confirmed by measuring the dependence of oscillation amplitude on increasing δ , as shown in Fig. 3(b), which matches well with theoretical predictions (see Supplementary Material for details), giving estimates of $\bar{C} = 3.6$ and $\bar{C} = 4.2$ from fits to ω_a and ω_c photodetected signals, respectively. This discrepancy in the cooperativities is attributed to non-ideal modulation when creating each probe and imbalance of the cooperativities of each mode.

We can also reconstruct the output of ζ_{dk} and ζ_{br} by inferring a and c from the measured phase and amplitude of the output probe fields in Fig. 3(a). This reconstruction requires the additional step of accounting for a slight phase shift due to differing optical path lengths at ω_a and ω_c caused by dispersion in the experimental setup, whose effect can be seen in the inset of Fig. 3(a). This deleterious phase shift was corrected in post-processing while determining ζ_{br} and ζ_{dk} . An example of the reconstructed bright and dark mode intensity is shown in Fig. 3(c), where flopping between the bright and dark state is evident. Notably, a difference in maximum intensity of ζ_{dk} and ζ_{br} is evident from their differing peak values. This difference can be related to the energy dissipated by the bright state due to its interaction with

the mechanical resonance, and is found from Eq. (2) generalized for non-zero δ (see Supplementary Material) to scale as $(1 + \bar{C}/(1 + 4(\delta/\gamma_b)^2))^{-2}$. Additional measurements of the intensity of a , c , ζ_{br} , and ζ_{dk} as a function of δ and time are plotted in Figs. 3(d–g), which clearly show how the oscillation period decreases with increasing δ , as expected theoretically.

TWO-COLOR SWITCHING

The phase-dependent response of this multicolor DOMIT system, together with our ability to selectively excite ζ_{dk} or ζ_{br} , can be harnessed to create a novel form of a phase-dependent all-optical switch. In this device the output intensity of one probe is dependent on the phase of the other probe, and follows the truth table of an XOR gate with probe field phases of 0 and π mapping onto boolean values 0 and 1. The maximum contrast achievable is determined by the maximum OMIT dip depth, and is given by $\bar{C}^2/(1 + \bar{C})^2$. This indicates that, in principle, the contrast can be made to approach unity for systems with large cooperativity.

This switching action can be inferred from Figs. 2(a,b), and directly observed in the time domain by varying the phase ϕ_c of the mode c probe following a temporal step function, while maintaining constant phase ϕ_a of the mode a probe, as sketched in Fig. 4(a) for switching off and Fig. 4(b) for switching on. Experimental time domain data showing the resulting change in probe a transmission is shown in Figs. 4(c,d). As mentioned above, the relative phase $\phi = \phi_a - \phi_c$ is controlled by introducing an electrical phase delay in the RF signal driving the electro-optic modulator responsible for creating the mode c probe (see Supplementary Material for de-

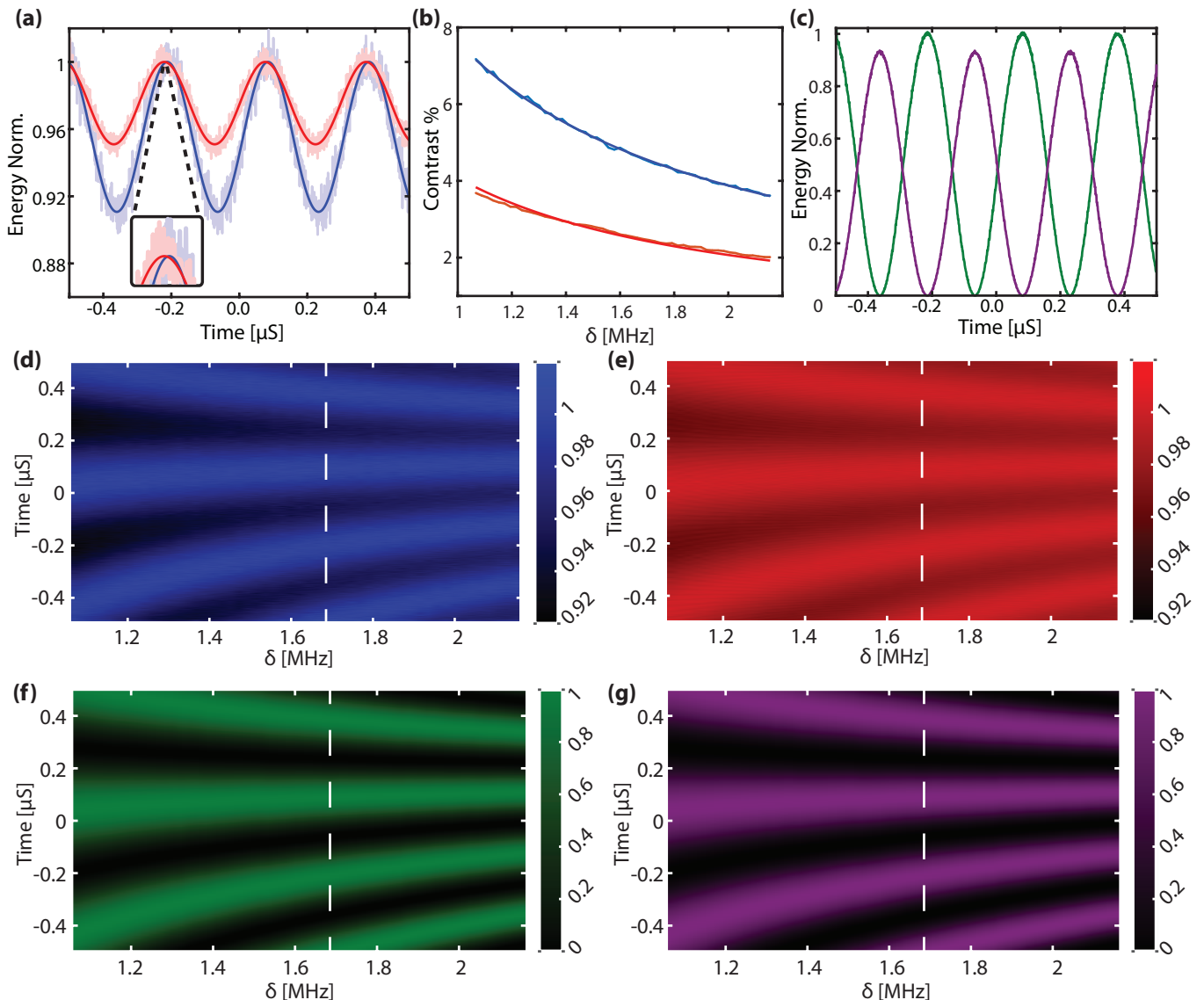


FIG. 3: (a) Example of the oscillations in stored energy in mode a (blue trace) and mode c (red trace) for $2\delta = 3.37$ MHz, measured by downmixing the heterodyne signal at each color in the time domain to isolate each probe amplitude. Inset: highlight of the slight time delay between the output of modes a and c caused by dispersion in the setup. (b) Amplitude of the oscillations for mode a (blue) and mode c (red) as a function of δ , and corresponding predictions from the model given in the text. (c) Normalized bright (purple) and dark (green) state energy for $2\delta = 3.37$ MHz, as inferred from the optical output of modes a and c shown in (a). (d-g) Oscillations as a function of time and δ of outputs from modes a , c , ζ_{br} , and ζ_{dk} respectively.

tails). The rapid oscillations are due to beating between the probe and control laser, whereas the oscillation envelope is proportional to the amplitude of the transmitted probe. From this upper envelope, shown in Figs. 4(e,f), we can measure the switch response speeds: fits with an exponential function yield fall and rise times of $0.73 \mu\text{s}$ and $0.88 \mu\text{s}$ respectively. Assuming that $\kappa_{a,c} \gg \gamma_b$, the switching speed can be shown to be $\tau^{-1} = \gamma_b(1 + \bar{C})$, which approaches zero for sufficiently large \bar{C} . This switching speed implies $\bar{C} = 2.96$ and $\bar{C} = 3.89$ respectively, for the fall and rise times illustrated in Figs. 4(c,d), consistent with expectations for the control field ampli-

tudes. The observed differences in the fall and rise times are presumed to be due to differences in intracavity control field amplitudes during the respective measurements.

CONCLUSION

In summary, we demonstrate coherent interference between spectrally-separated optical modes mediated by optomechanical coupling. By adjusting the phase between different color probe fields entering the cavity, we selectively excite either a mechanically bright or a me-

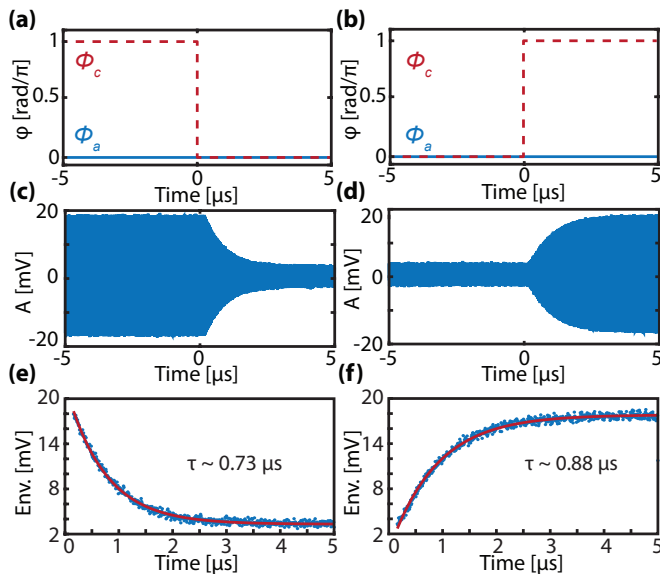


FIG. 4: (a,b) Phases of the input probe fields vs. time which cause probe c to switch the response of probe a off and on, respectively. (c,d) Photodetected cavity output of probe a when the input phase of probe c is switched temporally as shown in (a) and (b). The rapid oscillations are caused by beating between the control and probe, and the envelope reveals the action of the switch. (e,f) Envelope extracted from the peak values of the data in (c,d) and fit with exponentially falling and rising functions, respectively.

mechanically dark mode, and demonstrate controllable coupling between the two modes. Notably, we exploit difference between bright- and dark-state transmission to demonstrate a novel two-color, all-optical switch, where the control and target are at different wavelengths.

Our system has great potential for applications to quantum information processing where interference between frequency binned qubits is desirable [6], such as frequency-domain Hong-Ou-Mandel interference [12, 13], chromatic and time-domain interferometry [5, 14, 39], and microwave-to-optical conversion via the optomechanical dark mode [25]. As the diamond devices studied here have high-quality optical modes in the visible spectrum [5], interference between telecommunication wavelength light and light resonant with quantum emission from diamond nitrogen vacancy (637 nm) and silicon vacancy (736 nm) color centers will be feasible in future studies, providing a path towards linking quantum networking components. Furthermore, our technique could be extended to many optical modes, without the stringent phase matching requirements of nonlinear optics; thus, our technique could lead to many-color interference processes. Finally, we note that this interference is quite general and could be utilized for non-optical inputs such as magnetic or electric fields, provided they couple to the mechanical degree of freedom. Future experiments operating in the quantum domain will benefit from cryogenic pre-cooling of the device to its mechanical quantum ground state, which is achievable at dilution fridge tem-

peratures for the > 2 GHz frequency mechanical mode measured in this report.

* pbarclay@ucalgary.ca

- [1] B. Abbott, *et al.*, *Phys. Rev. Lett.* **118**, 221101 (2017).
- [2] A. Yariv, P. Yeh, *Photonics: Optical Electronics in Modern Communications* (Oxford, New York, 2006).
- [3] A. Liu, *et al.*, *Nature* **427**, 615 (2004).
- [4] J. O'Brien, A. Furusawa, J. Vučković, *Nat. Photonics* **3**, 687 (2009).
- [5] S. Clemmen, A. Farsi, S. Ramelow, A. L. Gaeta, *Phys. Rev. Lett.* **117**, 223601 (2016).
- [6] H.-H. Lu, *et al.*, *Optica* **5**, 1455 (2018).
- [7] M. Kues, *et al.*, *Nature* **546**, 622 (2017).
- [8] G. Kurizki, *et al.*, *Proceedings of the National Academy of Sciences* **112**, 3866 (2015).
- [9] S. Harris, Y. Yamamoto, *Phys. Rev. Lett.* **81**, 3611 (1998).
- [10] D. E. Chang, V. Vuletić, M. D. Lukin, *Nat. Photonics* **8**, 685 (2014).
- [11] H. J. McGuinness, M. G. Raymer, C. J. McKinstrie, S. Radic, *Phys. Rev. Lett.* **105**, 093604 (2010).
- [12] T. Kobayashi, *et al.*, *Nat. Photon.* **10**, 441 (2016).
- [13] Q. Li, *et al.*, *arXiv:1905.01698* (2019).
- [14] L.-Y. Qu, *et al.*, *arXiv:1905.01823 [quant-ph]* (2019).
- [15] M. Aspelmeyer, T. J. Kippenberg, F. Marquardt, *Rev. Mod. Phys.* **86**, 1391 (2014).
- [16] A. H. Safavi-Naeini, *et al.*, *Nature* **472**, 69 (2011).
- [17] S. Weis, *et al.*, *Science* **330**, 1520 (2010).
- [18] V. Fiore, C. Dong, M. C. Kuzyk, H. Wang, *Phys. Rev. A* **87**, 023812 (2013).
- [19] S. E. Harris, *Phys. Today* **50**, 36 (1997).
- [20] J. T. Hill, A. H. Safavi-Naeini, J. Chan, O. Painter, *Nat. Commun.* **3**, 1196 (2012).
- [21] C. Dong, V. Fiore, M. C. Kuzyk, H. Wang, *Science* **338**, 1609 (2012).
- [22] Y. Liu, M. Davanço, V. Aksyuk, K. Srinivasan, *Phys. Rev. Lett.* **110**, 223603 (2013).
- [23] C. Ockeloen-Korppi, *et al.*, *Phys. Rev. X* **6**, 041024 (2016).
- [24] S. Barzanjeh, *et al.*, *arXiv:1809.05865* (2018).
- [25] K. C. Balram, M. I. Davanço, J. D. Song, K. Srinivasan, *Nat. Photonics* **10**, 346 (2016).
- [26] E. Korsunsky, N. Leinfellner, A. Huss, S. Balushev, L. Windholz, *Phys. Rev. A* **59**, 2302 (1999).
- [27] B. Kim, B.-U. Sohn, W. Shin, D.-K. Ko, H. Kang, *J. Opt. Soc. Am. B* **32**, 227 (2015).
- [28] H. Xu, D. Mason, L. Jiang, J. Harris, *Nature* **537**, 80 (2016).
- [29] M. C. Kuzyk, H. Wang, *Phys. Rev. A* **96**, 023860 (2017).
- [30] M. Zhang, L. Wang, P. Ye, *IEEE Commun. Mag.* **43**, S19 (2005).
- [31] Y.-D. Wang, A. A. Clerk, *Phys. Rev. Lett.* **108**, 153603 (2012).
- [32] L. Tian, *Phys. Rev. Lett.* **108**, 153604 (2012).
- [33] S. J. Buckle, S. M. Barnett, P. L. Knight, M. A. Lauder, D. T. Pegg, *Optica Acta: International Journal of Optics* **33**, 1129 (1986).
- [34] D. V. Kosachiov, B. G. Matisov, Y. V. Rozhdestvensky, *J. Phys. B.* **25**, 2473 (1992).

- [35] T. Palomaki, J. Harlow, J. Teufel, R. Simmonds, K. Lehnert, *Nature* **495**, 210 (2013).
- [36] M. C. Kuzyk, H. Wang, *Phys. Rev. A* **96**, 023860 (2017).
- [37] M. Mitchell, *et al.*, *Optica* **3**, 963 (2016).
- [38] D. P. Lake, M. Mitchell, Y. Kamaliddin, P. E. Barclay, *ACS Photonics* **5**, 782 (2018).
- [39] D. V. Reddy, M. G. Raymer, *Optica* **5**, 423 (2018).

SUPPLEMENTARY INFORMATION

EXPERIMENT SETUP AND CALIBRATION

The optomechanical cavity utilized in this work is a single-crystal diamond (SCD) microdisk, fabricated according to the process outlined in Refs. [S1, S2], an example of which is shown in Fig. S1(a). An advantage of microdisk cavities is that they support multiple optical whispering gallery modes across their transparency window, all of which exhibit dispersive optomechanical coupling to the fundamental radial breathing mode (RBM) of the microdisk [S3], as illustrated schematically in Fig. S1(b). Diamond's large electronic bandgap, Young's modulus, and best-in-class thermal conductivity make it an ideal material for use in cavity optomechanics as it can support large intracavity photon number N , and high optical and mechanical quality factors. Additionally, color center qubits present in diamond, such as silicon and nitrogen vacancies, make it a promising platform for realizing hybrid quantum systems [S4].

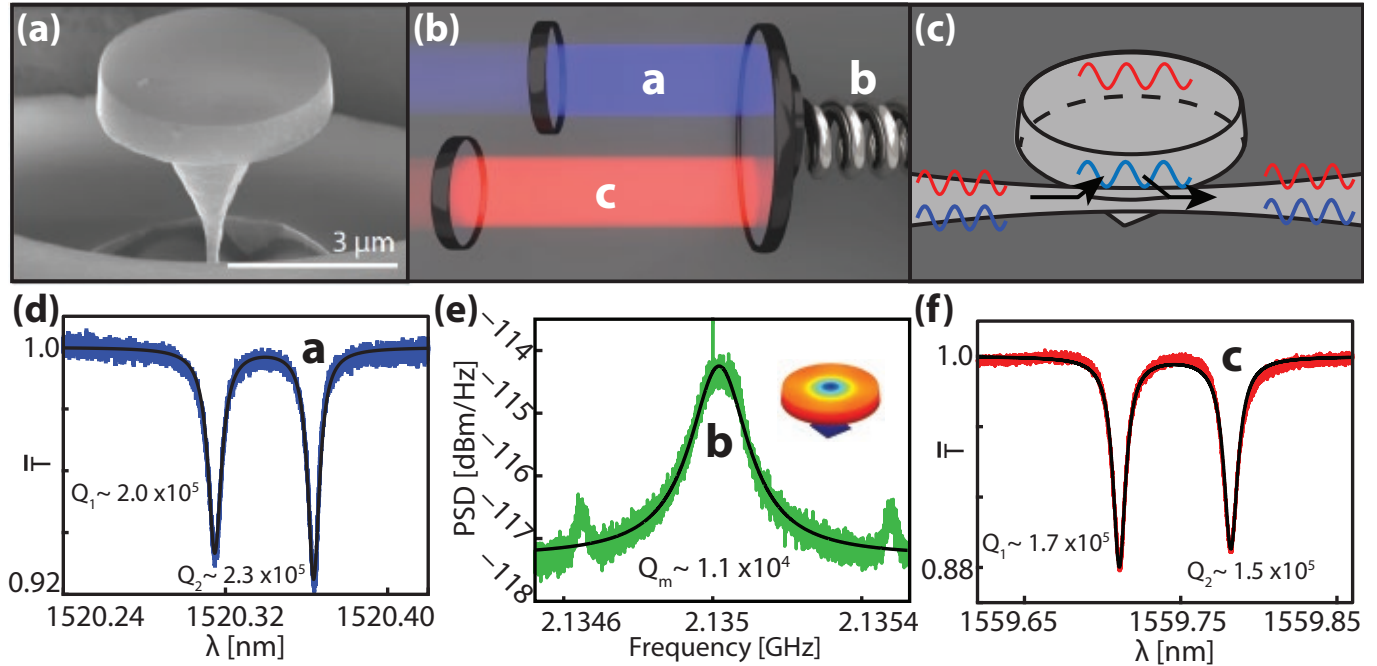


FIG. S1: (a) Scanning electron micrograph of a diamond microdisk similar to the one used in this work. (b) Cartoon of a canonical multimode optomechanical system. Here mode b , represented as a spring, is dispersively coupled to both optical modes a and c . (c) Cartoon of fiber taper-microdisk coupling. (d) Normalized fiber taper transmission scan of mode a used in this experiment, with fit. (e) Power spectral density of the fiber taper transmission when the input laser is tuned near a cavity mode, revealing fluctuations from thermomechanical motion of the cavity's mechanical radial breathing mode, b . A COMSOL simulated displacement field profile of the radial breathing mode is shown in the inset. (f) Normalized fiber taper transmission scan of optical mode c , with fit.

Light from two tunable diode lasers was coupled into and out of the microdisk using a dimpled optical fiber taper positioned adjacent to the microdisk as illustrated in the cartoon in Fig. S1(c). The spatial overlap of the evanescent field of the fiber and the optical modes of the microdisk permit efficient coupling, allowing measurement of cavity modes in transmission and reflection. Two telecommunications wavelength modes at $\lambda_a = 2\pi c/\omega_a = 1520$ nm and $\lambda_c = 2\pi c/\omega_c = 1560$ nm were selected for this work, as they were in the operating range of the available lasers (Newport TLB-6700) and optical amplifier (Pritel EDFA). However, this could be extended to visible wavelengths, where these devices have demonstrated high quality optical modes [S5]. The optical modes are each dispersively coupled to the microdisk's fundamental mechanical radial breathing mode (RBM) whose frequency is $\omega_b/2\pi = 2.1$ GHz, with vacuum optomechanical coupling rates, $g_{0,a}, g_{0,c} \sim 2\pi \times 25$ kHz. Measurements of the fiber taper optical transmission spectrum for wavelengths scanned across modes a and c are shown on Figs. S1(d,f), and the power spectral density of the fluctuations imparted on photodetected output due to thermally driven mechanical motion of the RBM when the input laser is tuned close to resonance with an optical mode [S6-S8] is shown on Fig. S1(e). Note that both optical modes are standing wave doublets due to surface roughness induced coupling between the clockwise and counterclockwise propagating whispering gallery modes of the microdisks [S9]. For all of the measurements

presented here the long wavelength doublet mode was used, and the lower wavelength doublet mode was assumed to not influence the observed phenomena. This device operates in the sideband resolved regime, $\omega_b \gg \kappa_a, \kappa_c$, where $\kappa_a/2\pi \sim 0.87$ GHz, and $\kappa_c/2\pi \sim 1.20$ GHz are the energy decay rates of the optical modes.

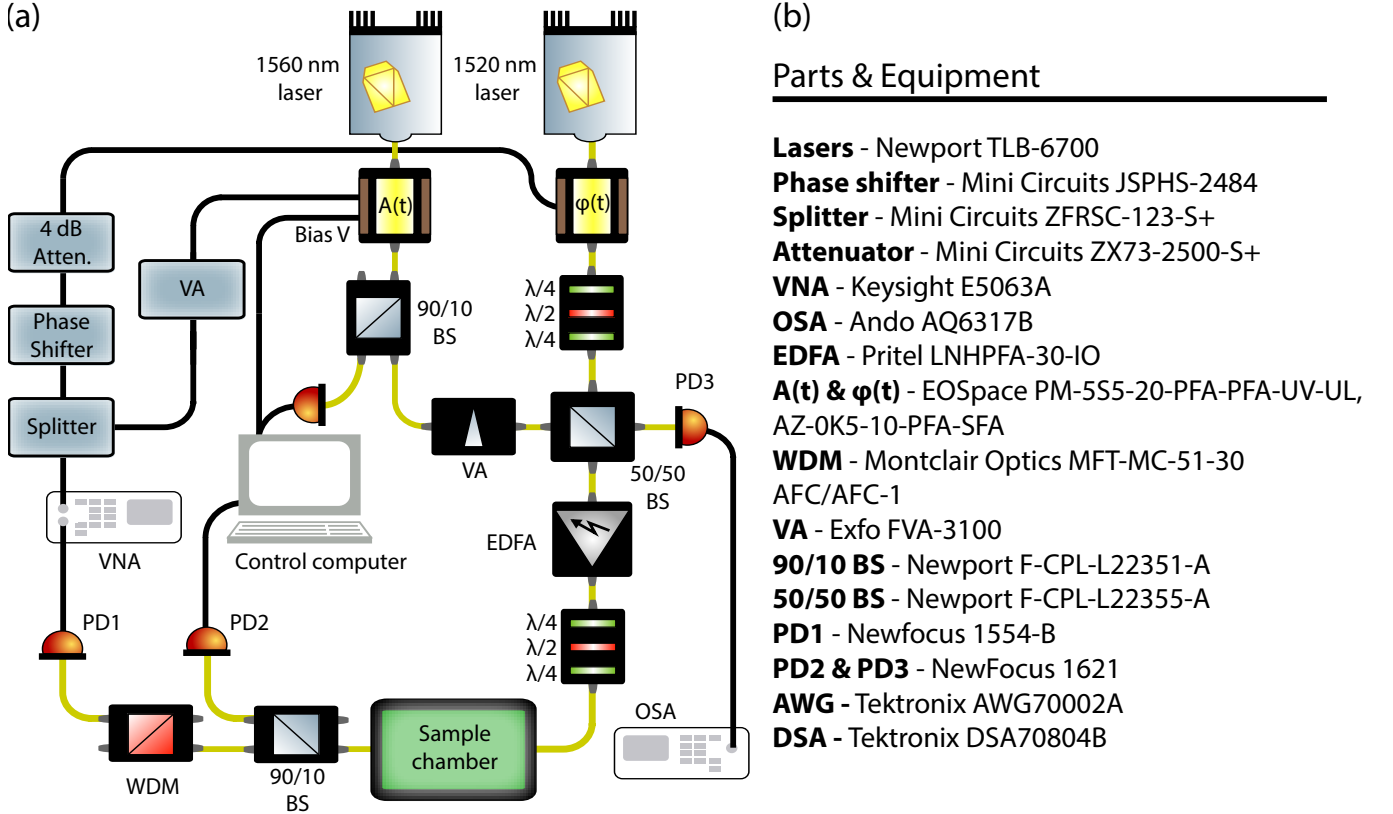


FIG. S2: (a) Setup used in the experiments. The Vector Analyzer (VNA) acted as the RF source for modulators on each path. The resulting signal was spectrally filtered to isolate for the mode of interest. Key: OSA (Optical spectrum analyzer), BS (Beam splitter), VA (Variable attenuator), BS (Beam splitter), EDFA (Erbium doped fiber amplifier), WDM (Wavelength division multiplexer), PD (Photodetector). (b) Parts and equipment used in the experiment.

Figure S2 shows a schematic representation of the experimental setup used for the above measurements and those shown in the main text. To measure the optomechanically induced transparency (OMIT) spectra of each mode, sidebands were created on each respective control laser for use as probe lasers, using either phase, $\phi(t)$, or amplitude, $A(t)$, electro-optic modulators. For the data in Fig. 2 of the main text, the electrical RF drive for each modulator was derived from the same vector network analyzer (VNA), with one path undergoing a controllable phase shift relative to the other. This controllable phase shift was achieved by placing an electronic phase shifter before one of the electro-optic modulators (EOMs), shown in Fig. S2(a). Because the phase shifter transmission varied as a function of phase, a variable electrical attenuator was calibrated and used to maintain balance between the probe laser powers at every step in phase, by controlling the RF modulation amplitude. An optical variable attenuator (VA) was used on the 1560 nm laser arm to attempt to balance the input power of each laser before they were combined via a 50/50 waveguide coupler, and amplified with an erbium doped amplifier (EDFA) before being routed to the sample chamber (a nitrogen purged enclosure) and device. The other output of the 50/50 coupler was used to perform slow laser wavelength locking via a photodetector (PD) and optical spectrum analyzer (OSA) connected to the control computer. The signal exiting the sample chamber was then divided on a 90/10 waveguide coupler. The 10% port was routed to a low speed PD for use in measuring the cavity transmission during the initial setup, and the 90% port was sent to the wavelength division multiplexer (WDM). By connecting the WDM to a high-speed photodetector, the output of either mode a or c could be selected.

For the bright–dark mode coupling experiment (Fig. 3 in the main text) and the time domain switch (Fig. 4 in the main text), a two–channel arbitrary waveform generator (AWG) was used as the RF source, with one channel assigned to each modulator. Acquisition was performed using a digital spectrum analyzer (DSA), which was triggered by the AWG. To isolate the beat note between the probe field of one mode and the converted probe from the other mode

the signal acquired on the DSA was digitally downmixed post-acquisition.

ELECTRO-OPTIC MODULATION AND PROBE MEASUREMENT MODEL

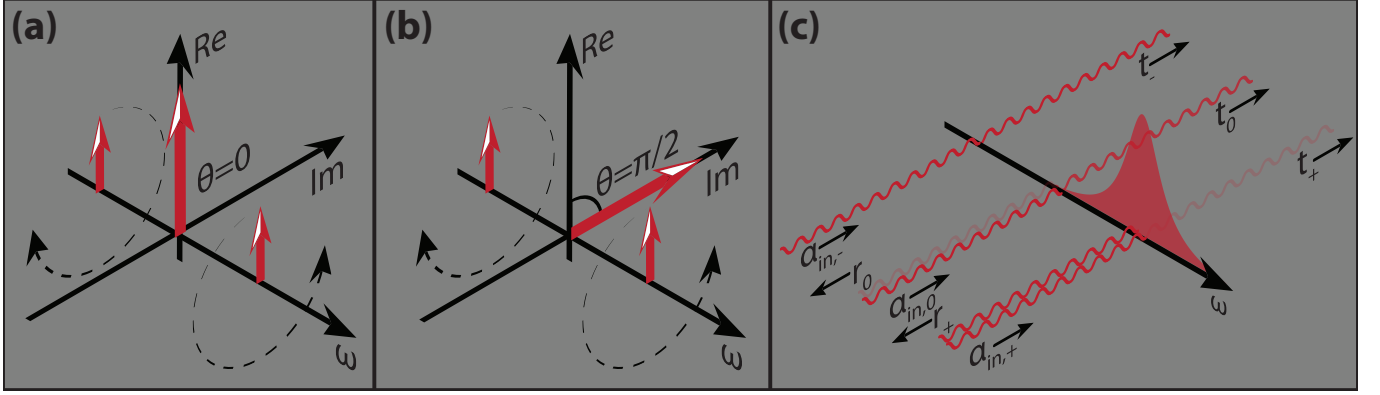


FIG. S3: (a) Frequency components of pure amplitude modulation in a frame rotating at the carrier frequency. The two sidebands are placed at $\pm\omega_m$, where ω_m is the frequency of modulation. Here the modulation is in a direction parallel to the carrier tone. (b) Frequency components of a pure phase modulation. Unlike the case of amplitude modulation, the modulation occurs in a direction perpendicular to the carrier tone. (c) Illustration of the expected reflected and transmitted signals for the case of a red detuned pump laser modulated such that one sideband is near resonance with the cavity.

The results demonstrated here require strong control fields and weak probe fields, which were generated through EOM modulation of the control fields. Due to the available equipment, a phase EOM was used for the mode near ω_a and an amplitude EOM for the mode near ω_c . This leads to differences in the probe transduction as measured on the high speed PD.

For weak modulation ($\beta \ll 1$, where β is the index of modulation), we can assume the output of the EOM has three distinct frequency components at ω , $\omega \pm \omega_m$, where ω is the frequency of the carrier tone and ω_m is the frequency of modulation. For convenience we will work in a frame rotating with the carrier at ω . The type of modulation can be inferred from the sum of the sideband components in the imaginary plane. For pure amplitude modulation they will oscillate parallel to the carrier with frequency ω_m , whereas for pure phase modulation they will oscillate perpendicular to the carrier as illustrated in Fig. S3(a,b). We note that since we are working in the rotating frame, we can choose the phase of the carrier out of convenience, as only the relative phase between the sidebands and the carrier tone influences the result.

In practice, the construction of amplitude EOMs is often such that the chirp is non-zero, which results in non-zero phase modulation of the outgoing field. With this in mind, we can write the transmission of the modulated field through the cavity as $|\alpha_{out}\rangle = t|\alpha_{in}\rangle$, where

$$t = \text{diag}\{t_+, t_0, t_-\}, |\alpha_{in}\rangle = \alpha_{in}^0 \left(\frac{\beta}{2} e^{-i\omega_m t}, e^{i\theta}, \frac{\beta}{2} e^{i\omega_m t} \right)^T. \quad (\text{S1})$$

In the previous expression, t_+ , t_0 , t_- are the transmission coefficients at the upper sideband, carrier frequency, and lower sideband, respectively. The angle between the sidebands and the carrier is θ , where $\theta = n\pi$ for a pure amplitude modulator and $\theta = \pi/2 \pm n\pi$ for a pure phase modulator, where n is an integer.

The frequency components of the field transmitted through the cavity can be projected using the matrices

$$\mathbf{P}_+ = \begin{pmatrix} 0 & 1 & 0 \\ 0 & 0 & 1 \\ 0 & 0 & 0 \end{pmatrix}, \mathbf{P}_0 = \begin{pmatrix} 1 & 0 & 0 \\ 0 & 1 & 0 \\ 0 & 0 & 1 \end{pmatrix}, \mathbf{P}_- = \begin{pmatrix} 0 & 0 & 0 \\ 1 & 0 & 0 \\ 0 & 1 & 0 \end{pmatrix}. \quad (\text{S2})$$

Using the above expressions, we can write the signal measured on the PD up to a constant as $S = S_0 + S_1 + S_2$, where

$$S_0 = \langle \alpha_{out} | P_0 | \alpha_{out} \rangle, \quad (\text{S3})$$

$$S_1 \cos(\omega_m t + \phi_1) = \langle \alpha_{out} | P_+ | \alpha_{out} \rangle + \langle \alpha_{out} | P_- | \alpha_{out} \rangle, \quad (\text{S4})$$

$$S_2 \cos(2\omega_m t + \phi_2) = \langle \alpha_{out} | P_+^2 | \alpha_{out} \rangle + \langle \alpha_{out} | P_-^2 | \alpha_{out} \rangle. \quad (\text{S5})$$

By electronic filtering we isolate the $\mathcal{O}(\omega_m)$ component of the signal, where

$$S_1 = \beta |t_0^* t_+ e^{-i\theta} + t_0 t_-^* e^{i\theta}|. \quad (\text{S6})$$

To find the expected signal when phase modulation dominates over amplitude modulation we take $\theta \approx \pm\pi/2 + \delta_\theta$, where δ_θ is small. In this work the control laser is red detuned from a sideband-resolved cavity, as illustrated in Fig. S3(c). In this case the lower sideband passes un-attenuated ($t_- = 1$, $r_- = 0$), and the control laser is approximately real $t_0 \approx t_0^*$. In this case, to first order in modulation angle, the expected signal is

$$S_1 \approx \beta t_0 \sqrt{|r_+|^2 + 2\delta_\theta \text{Im}\{r_+\}}, \quad (\text{S7})$$

where we have used the fact that $t_+ + r_+ = 1$. Using the chirp parameter [S10] specified by the manufacturer for the amplitude EOM we calculate $\delta_\theta = 0.35$ [rad]. Furthermore, in all experiments in this work the probe is sufficiently close to resonance such that r_+ is approximately real. Therefore, we conclude that regardless of the EOM used, $|S_1| \approx \beta t_0 |r_+| \propto |r_+| \propto |\alpha|$, where α is the cavity population.

DATA ANALYSIS

In order to examine the bright and dark state coupling as shown in Fig. 3 in the main text, time-domain data was directly acquired on the DSA. For this dataset we digitally down mixed by the carrier frequency ω_b , which allowed us to extract both the amplitude of the signal, and the phase relative to the carrier signal for modes a and c . Due to chirp in the amplitude modulator, dispersion in the fiber, and difference in the optical path length of the two output arms of the WDM, a delay between the mode outputs was observed. To correct for this we fit the oscillating output of each mode to a sinusoidal function, and subtract the phase difference. Using this we are able to reconstruct the output of the dark and bright states.

DOUBLE OPTOMECHANICALLY INDUCED TRANSPARENCY

In this work, two optical modes a and c exhibit dispersive optomechanical coupling to the mechanical mode b . We denote the frequencies of these modes as ω_a , ω_c , and ω_b , respectively, and the vacuum optomechanical coupling rates as g_a , and g_c . This is modelled by the Hamiltonian $\hat{H} = \hat{H}_0 + \hat{H}_{\text{int}}$, where \hat{H}_0 describes the internal dynamics of each mode and \hat{H}_{int} is the interaction Hamiltonian

$$\begin{aligned} \hat{H}_0 &= \hbar\omega_a \hat{a}^\dagger \hat{a} + \hbar\omega_b \hat{b}^\dagger \hat{b} + \hbar\omega_c \hat{c}^\dagger \hat{c}, \\ \hat{H}_{\text{int}} &= -\hbar g_a \hat{a}^\dagger \hat{a} (\hat{b} + \hat{b}^\dagger) - \hbar g_c \hat{c}^\dagger \hat{c} (\hat{b} + \hat{b}^\dagger). \end{aligned} \quad (\text{S8})$$

We describe the coupling between the optical modes and a waveguide using input-output theory

$$\begin{aligned} \dot{\hat{a}} &= \frac{i}{\hbar} [\hat{H}, \hat{a}] - \frac{\kappa_a}{2} \hat{a} + \sqrt{\kappa_a^{\text{ex}}} \hat{a}_{\text{in}}, \\ \dot{\hat{c}} &= \frac{i}{\hbar} [\hat{H}, \hat{c}] - \frac{\kappa_c}{2} \hat{c} + \sqrt{\kappa_c^{\text{ex}}} \hat{c}_{\text{in}}, \end{aligned} \quad (\text{S9})$$

where \hat{a}_{in} and \hat{c}_{in} are the input field operators for each optical mode, and κ_a , κ_c and κ_a^{ex} , κ_c^{ex} are the total energy decay and waveguide-cavity coupling rates of mode a and c , respectively. Note that in this work the cavity is double-sided and consequently the cavity-waveguide coupling rate in each direction is $\kappa_{\text{ex}}/2$.

For all scenarios described in this work control lasers were red-detuned from the cavity modes whereas probe lasers were tuned near resonance. Although the modulators create multiple sidebands, the spectral selectivity of the cavity is such that only one sideband will contribute to the physics of the problem. This allows us to linearize about the control fields using the substitutions $\hat{a} \rightarrow \alpha_a + \hat{a}$, and $\hat{c} \rightarrow \alpha_c + \hat{c}$, where α_a, α_c are the classical control fields amplitudes, and \hat{a}, \hat{c} now represent the cavity fluctuations near the probe frequencies. We also use similar substitutions for the input field amplitudes, such that \hat{a}_{in} and \hat{c}_{in} are the input probe field operators. Neglecting small order terms, and accounting for a static mechanical shift induced by constant radiation pressure, our interaction Hamiltonian becomes

$$\hat{H}_{\text{int}} = -\hbar g_a (\alpha_a \hat{a}^\dagger + \alpha_a^* \hat{a}) (\hat{b} + \hat{b}^\dagger) - \hbar g_c (\alpha_c \hat{c}^\dagger + \alpha_c^* \hat{c}) (\hat{b} + \hat{b}^\dagger). \quad (\text{S10})$$

We consider the case where the control lasers are red-detuned, with the probe fields on resonance such that $\Delta_i^{\text{ctrl}} = \omega_i^{\text{ctrl}} - \omega_i = -\omega_b$, and $\omega_i^{\text{probe}} - \omega_i^{\text{ctrl}} = \omega_b$, where $i = \{a, c\}$. In this case, selecting only the resonant terms under the rotating wave approximation, the above expression simplifies to

$$\hat{H}_{\text{int}} = -\hbar \left(G_a \hat{a}^\dagger \hat{b} + G_a^* \hat{a} \hat{b}^\dagger + G_c \hat{c}^\dagger \hat{b} + G_c^* \hat{c} \hat{b}^\dagger \right), \quad (\text{S11})$$

where $G_a = \alpha_a g_a$ and $G_c = \alpha_c g_c$. Transforming into frequency space, in a frame rotating with the control lasers, and making use of Eqs. S9 and S11 we may solve for the mode operators using the set of coupled linear equations

$$\begin{bmatrix} \chi_a^{-1}(\omega) & -iG_a & 0 \\ -iG_a^* & \chi_b^{-1}(\omega) & -iG_c^* \\ 0 & -iG_c & \chi_c^{-1}(\omega) \end{bmatrix} \begin{bmatrix} \hat{a} \\ \hat{b} \\ \hat{c} \end{bmatrix} = \begin{bmatrix} \sqrt{\kappa_a^{\text{ex}}} \hat{a}_{\text{in}} \\ \sqrt{\gamma_b} \hat{b}_{\text{in}} \\ \sqrt{\kappa_c^{\text{ex}}} \hat{c}_{\text{in}} \end{bmatrix}. \quad (\text{S12})$$

In the above we have written the cavity susceptibilities as $\chi_a^{-1}(\omega) = \kappa_a/2 - i(\Delta_a + \omega)$, and $\chi_c^{-1}(\omega) = \kappa_c/2 - i(\Delta_c + \omega)$, where, for notational cleanliness we have defined $\Delta_a = \Delta_a^{\text{ctrl}}$, and $\Delta_c = \Delta_c^{\text{ctrl}}$. We also define the mechanical susceptibility as $\chi_b^{-1}(\omega) = \gamma_b/2 - i(-\omega_b + \omega)$, including a mechanical input field, \hat{b}_{in} , which can be used to model thermal contact with the environment.

From here the solutions become tractable if we make a change of basis to symmetric and antisymmetric combinations of the a and c modes which we refer to as the optomechanically dark, ζ_{dk} , and bright, ζ_{br} , modes [S11]

$$\hat{\zeta}_{\text{dk}} = \frac{G_c \hat{a} - G_a \hat{c}}{i\bar{G}}, \quad (\text{S13})$$

$$\hat{\zeta}_{\text{br}} = \frac{G_a^* \hat{a} + G_c^* \hat{c}}{\bar{G}}, \quad (\text{S14})$$

where

$$\bar{G} = \sqrt{|G_a|^2 + |G_c|^2}. \quad (\text{S15})$$

Assuming $\kappa_1 = \kappa_2 = \kappa$, and $\Delta_a = \Delta_c = \Delta$, we arrive at de-coupled equations of motion, which have the solutions

$$\hat{\zeta}_{\text{dk}} = \frac{1}{\kappa/2 - i(\Delta + \omega)} \left(\frac{\sqrt{\kappa_a^{\text{ex}}} G_c \hat{a}_{\text{in}} - \sqrt{\kappa_c^{\text{ex}}} G_a \hat{c}_{\text{in}}}{i\bar{G}} \right), \quad (\text{S16})$$

$$\hat{b} = \frac{1}{\gamma_b/2 - i(-\omega_b + \omega)} \left(\sqrt{\gamma_b} \hat{b}_{\text{in}} + i\bar{G} \hat{\zeta}_{\text{br}} \right), \quad (\text{S17})$$

$$\hat{\zeta}_{\text{br}} = \frac{1}{\kappa/2 - i(\Delta + \omega) + \frac{\bar{G}^2}{\gamma_b/2 - i(-\omega_b + \omega)}} \left(\frac{\sqrt{\kappa_a^{\text{ex}}} G_a^* \hat{a}_{\text{in}} + \sqrt{\kappa_c^{\text{ex}}} G_c^* \hat{c}_{\text{in}}}{\bar{G}} + \frac{i\bar{G} \sqrt{\gamma_b} \hat{b}_{\text{in}}}{\gamma_b/2 - i(-\omega_b + \omega)} \right). \quad (\text{S18})$$

To easily access the physics of the system we take $G_a = G_c = G$, and $\kappa_a^{\text{ex}} = \kappa_c^{\text{ex}} = \kappa_{\text{ex}}$ to simplify these expressions. We also explicitly include the phase difference between the probe fields, ϕ , and ignore any input mechanical drive, $\hat{b}_{\text{in}} \rightarrow 0$. Finally, we assume classical probe fields of equal amplitude, s_{in} , and drive each modulator at the same frequency, resulting in

$$\hat{\zeta}_{\text{dk}} = \frac{\sqrt{\kappa_{\text{ex}}} \sin(\phi/2) s_{\text{in}}}{\kappa/2 - i(\Delta + \omega)}, \quad (\text{S19})$$

$$\hat{\zeta}_{\text{br}} = \frac{\sqrt{\kappa_{\text{ex}}/2} \cos(\phi/2) s_{\text{in}}}{\kappa/2 - i(\Delta + \omega) + \frac{2G^2}{\gamma_b/2 - i(-\omega_b + \omega)}}. \quad (\text{S20})$$

DARK-BRIGHT MODE COUPLING

Up until this point, we have found no direct coupling between the bright and dark mode. However, by detuning either our probe or pump lasers in equal and opposite directions, we can induce a coupling between these two modes. To see this, we make the substitutions $\Delta_a \rightarrow \Delta + \delta$ and $\Delta_c \rightarrow \Delta - \delta$, assume that the input mechanical is negligible

($\hat{b}_{\text{in}} \rightarrow 0$), and set $G_a = G_c = G$, and $\kappa_1 = \kappa_2 = \kappa$ in Eqn. (4), which gives

$$\chi^{-1}(\omega)\hat{\zeta}_{\text{dk}} = \frac{\sqrt{\kappa_a^{\text{ex}}}\hat{a}_{\text{in}} - \sqrt{\kappa_c^{\text{ex}}}\hat{c}_{\text{in}}}{\sqrt{2}i} + \delta\hat{\zeta}_{\text{br}}, \quad (\text{S21})$$

$$\chi^{-1}(\omega)\hat{\zeta}_{\text{br}} = \frac{\sqrt{\kappa_a^{\text{ex}}}\hat{a}_{\text{in}} + \sqrt{\kappa_c^{\text{ex}}}\hat{c}_{\text{in}}}{\sqrt{2}} + i\overline{G}\hat{b} + \delta\hat{\zeta}_{\text{dk}}. \quad (\text{S22})$$

where $\chi^{-1}(\omega) = \kappa/2 - i(\Delta + \omega)$. From these expressions we see that there is coupling between bright and dark modes at a rate δ .

To describe this coupling in the time domain we first consider the intermodal coupling for the case $\delta = 0$, as illustrated in Fig. S4(a). Here, depending on the relative phase of the probe lasers, we arrive at a superposition of ζ_{br} and ζ_{dk} which is constant in time. In order for this process to remain stationary, we require interference to be between oscillations of the same frequency. From this, we can infer that by shifting the probe-cavity detuning by an amount δ , we cause interference to occur between differing frequencies, leading to beating between modes as illustrated in Fig. S4(b).

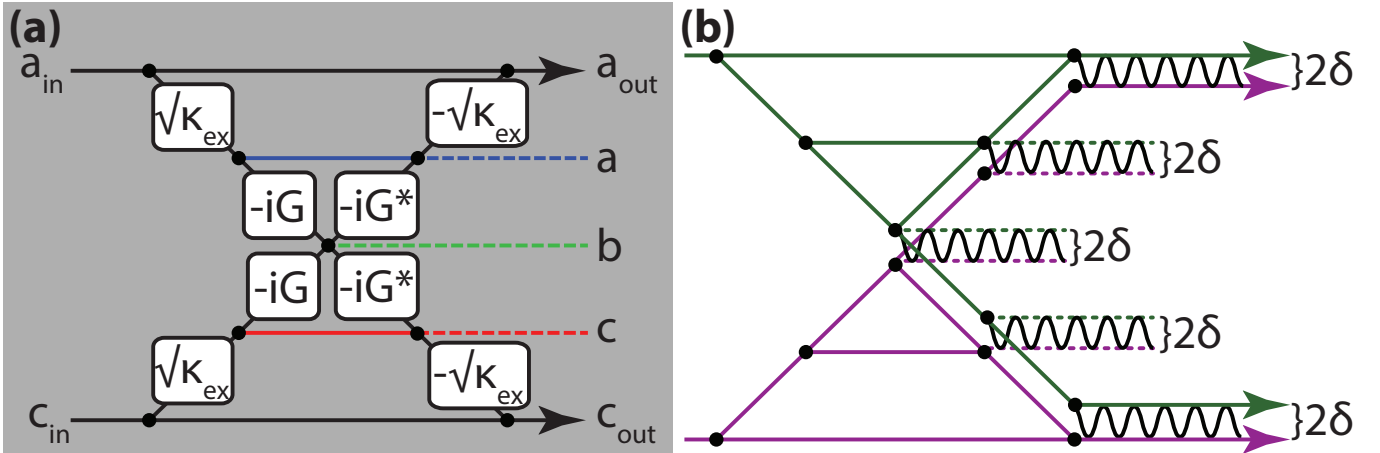


FIG. S4: (a) Intermodal coupling for the case of stationary DOMIT. Direction of propagation is left to right. (b) Effect of frequency shifting the control-probe detunings in opposite directions. Unlike the stationary case, we will observe a beating between all modes of the system.

To solve this, we divide each of modes into two frequency components at $\pm\delta$ of our original frequency terms as illustrated in Fig. S2(b). Considering first the dark state in the time domain, and choosing to set $\phi = 0$ for convenience, we find

$$\hat{\zeta}_{\text{dk}}(t) = \hat{\zeta}_{\text{dk}}^{(+)} + \hat{\zeta}_{\text{dk}}^{(-)} = \frac{e^{-i(\omega_b + \delta)t}}{\kappa/2 - i(\Delta + \omega_b + \delta)} \sqrt{\frac{\kappa_{\text{ex}}}{2}} \frac{s_{\text{in}}}{i} + \frac{e^{-i(\omega_b - \delta)t}}{\kappa/2 - i(\Delta + \omega_b - \delta)} \sqrt{\frac{\kappa_{\text{ex}}}{2}} \frac{s_{\text{in}}}{i}. \quad (\text{S23})$$

In a similar manner, we find that the bright state may be written as

$$\begin{aligned} \hat{\zeta}_{\text{br}}(t) &= \hat{\zeta}_{\text{br}}^{(+)} + \hat{\zeta}_{\text{br}}^{(-)} \\ &= \frac{e^{-i(\omega_b + \delta)t}}{\kappa/2 - i(\Delta + \omega_b + \delta) + \frac{|\overline{G}|^2}{\gamma_b/2 - i(-\omega_b + \omega_b + \delta)}} \sqrt{\frac{\kappa_{\text{ex}}}{2}} s_{\text{in}} - \frac{e^{-i(\omega_b - \delta)t}}{\kappa/2 - i(\Delta + \omega_b - \delta) + \frac{|\overline{G}|^2}{\gamma_b/2 - i(-\omega_b + \omega_b - \delta)}} \sqrt{\frac{\kappa_{\text{ex}}}{2}} s_{\text{in}}. \end{aligned} \quad (\text{S24})$$

Setting $\Delta = -\omega_b$, and assuming $\delta \ll \kappa$, we find

$$\hat{\zeta}_{\text{dk}}(t) = \frac{2\sqrt{\kappa_{\text{ex}}} \sin(\delta t) e^{-i\omega_b t} s_{\text{in}}}{\kappa}, \quad (\text{S25})$$

$$\hat{\zeta}_{\text{br}}(t) = \frac{2\sqrt{\kappa_{\text{ex}}} \cos(\delta t) e^{-i\omega_b t} s_{\text{in}}}{\kappa(1 + \frac{\overline{G}}{1+4(\delta/\gamma_b)^2})}. \quad (\text{S26})$$

This gives us the output fields as

$$a(t) = \frac{e^{-i\omega_b t}}{\sqrt{2}} (i \sin(\delta t) \zeta_{\text{dk}}(0) + \cos(\delta t) \zeta_{\text{br}}(0)), \quad (\text{S27})$$

$$c(t) = \frac{e^{-i\omega_b t}}{\sqrt{2}} (-i \sin(\delta t) \zeta_{\text{dk}}(0) + \cos(\delta t) \zeta_{\text{br}}(0)). \quad (\text{S28})$$

We note that near resonance, the amplitudes ζ_{dk} and ζ_{br} approach those calculated for steady state. For cases where we detuned away from the DOMIT transparency ($\delta \gg \gamma_b$), or for small cooperativities, the amplitudes of the dark and light state approach each other, and the visibility of oscillations goes to zero. Explicitly, the resonance contrast of the oscillations is found to be

$$V(\delta) = 1 - \sqrt{\frac{\gamma_b^2 + 4\delta^2}{\gamma_b^2(1+C)^2 + 4\delta^2}}. \quad (\text{S29})$$

SWITCHING

Although we previously found solutions in the frequency domain, it is instructive to reconsider the equations of motion in the time domain

$$\dot{\hat{a}} = (i\Delta_a - \kappa_a/2)\hat{a} + iG_a\hat{b} + \sqrt{\kappa_a^{\text{ex}}}\hat{a}_{\text{in}}, \quad (\text{S30})$$

$$\dot{\hat{b}} = (-i\omega_b - \gamma_b/2)\hat{b} + iG_a^*\hat{a} + iG_c^*\hat{c} + \sqrt{\gamma_b}\hat{b}_{\text{in}}, \quad (\text{S31})$$

$$\dot{\hat{c}} = (i\Delta_c - \kappa_c/2)\hat{c} + iG_c\hat{b} + \sqrt{\kappa_c^{\text{ex}}}\hat{c}_{\text{in}}. \quad (\text{S32})$$

For the devices used in our experiment, the decay rate of our optics is much faster than our mechanics ($\kappa_a, \kappa_c \gg \gamma$). With this in mind we can use adiabatic elimination, and set $\dot{\hat{a}} = 0, \dot{\hat{c}} = 0$, and solve for the mechanics as

$$\dot{\hat{b}} = \left(-i\omega_b - \gamma_b/2 + \frac{|G_a|^2}{i\Delta_a - \kappa_a/2} + \frac{|G_c|^2}{i\Delta_c - \kappa_c/2} \right) \hat{b} - \frac{iG_a^*\sqrt{\kappa_a^{\text{ex}}}\hat{a}_{\text{in}}}{i\Delta_a - \kappa_a/2} - \frac{iG_c^*\sqrt{\kappa_c^{\text{ex}}}\hat{c}_{\text{in}}}{i\Delta_c - \kappa_c/2} + \sqrt{\gamma_b}\hat{b}_{\text{in}}. \quad (\text{S33})$$

Using this expression we find that for $\Delta_a = \Delta_c = 0$, as in the experiment

$$\dot{\hat{b}} = -(i\omega_b + \tau^{-1})\hat{b} + \frac{2iG_a\sqrt{\kappa_a^{\text{ex}}}\hat{a}_{\text{in}}}{\kappa_a} + \frac{2iG_c\sqrt{\kappa_c^{\text{ex}}}\hat{c}_{\text{in}}}{\kappa_c} + \sqrt{\gamma_b}\hat{b}_{\text{in}}. \quad (\text{S34})$$

This gives the switching speed as $\tau^{-1} = \frac{\gamma_b}{2}(1 + C_a + C_c)$, where $C_j = 4G_j^2/\kappa_j\gamma_b$ is the optomechanical cooperativity and $j = \{a, c\}$.

Assuming travelling wave singlet modes, the transmission amplitudes through the switch are

$$t_{\text{br}} = \frac{2\kappa_{\text{ex}}}{\kappa} \frac{1}{1+C} - 1, \quad (\text{S35})$$

$$t_{\text{dk}} = \frac{2\kappa_{\text{ex}}}{\kappa} - 1. \quad (\text{S36})$$

* pbarclay@ucalgary.ca

- [S1] B. Khanaliloo, M. Mitchell, A. C. Hryciw, P. E. Barclay, *Nano Lett.* **15**, 5131 (2015).
- [S2] M. Mitchell, D. P. Lake, P. E. Barclay, *APL Photonics* **4**, 016101 (2019).
- [S3] D. P. Lake, M. Mitchell, Y. Kamaliddin, P. E. Barclay, *ACS Photonics* **5**, 782 (2018).
- [S4] I. Aharonovich, A. D. Greentree, S. Prawer, *Nat. Photonics* **5**, 397 (2011).
- [S5] M. Mitchell, *et al.*, *Optica* **3**, 963 (2016).
- [S6] T. J. Kippenberg, H. Rokhsari, T. Carmon, A. Scherer, K. J. Vahala, *Phys. Rev. Lett.* **95**, 033901 (2005).
- [S7] T. Carmon, H. Rokhsari, L. Yang, T. J. Kippenberg, K. J. Vahala, *Phys. Rev. Lett.* **94**, 223902 (2005).
- [S8] H. Rokhsari, T. J. Kippenberg, T. Carmon, K. J. Vahala, *Opt. Express* **13**, 5293 (2005).
- [S9] T. J. Kippenberg, S. M. Spillane, K. J. Vahala, *Opt. Lett.* **27**, 1669 (2002).
- [S10] L.-S. Yan, Q. Yu, A. E. Willner, Y. Shi, *Opt. Lett.* **28**, 1114 (2003).
- [S11] C. Dong, V. Fiore, M. C. Kuzyk, H. Wang, *Science* **338**, 1609 (2012).